AGU PUBLICATIONS

JGR

Journal of Geophysical Research: Atmospheres

RESEARCH ARTICLE
10.1002/2017JD026672

Key Points:
- Thermal wind imbalance in the exit region of the jet streak resulted in a mesoscale jetlet in the lee of the mountains
- Thermally direct transverse ageostrophic circulation in the exit region of the jetlet led to the upward motion and adiabatic expansion
- Low-level pressure rise generated the ageostrophic isallobaric wind that advected cold air toward the thermally induced low pressure area

Correspondence to:
A. K. Pokharel,
ashokpokharel@hotmail.com

Citation:
Pokharel, A. K., Kaplan, M. L., & Fiedler, S. (2017). The role of jet adjustment processes in subtropical dust storms. *Journal of Geophysical Research: Atmospheres*, *122*, 12,122–12,139. https://doi.org/10.1002/2017JD026672

Received 22 FEB 2017
Accepted 30 OCT 2017
Accepted article online 3 NOV 2017
Published online 20 NOV 2017

The Role of Jet Adjustment Processes in Subtropical Dust Storms

Ashok Kumar Pokharel[1,2], Michael L. Kaplan[2], and Stephanie Fiedler[3]

[1]Department of Atmospheric Sciences, University of Nevada, Reno, NV, USA, [2]Division of Atmospheric Science, Desert Research Institute, Reno, NV, USA, [3]Max-Planck-Institute for Meteorology, Hamburg, Germany

Abstract Meso-α/β/γ scale atmospheric processes of jet dynamics responsible for generating Harmattan, Saudi Arabian, and Bodélé Depression dust storms are analyzed with observations and high-resolution modeling. The analysis of the role of jet adjustment processes in each dust storm shows similarities as follows: (1) the presence of a well-organized baroclinic synoptic scale system, (2) cross mountain flows that produced a leeside inversion layer prior to the large-scale dust storm, (3) the presence of thermal wind imbalance in the exit region of the midtropospheric jet streak in the lee of the respective mountains shortly after the time of the inversion formation, (4) dust storm formation accompanied by large magnitude ageostrophic isallobaric low-level winds as part of the meso-β scale adjustment process, (5) substantial low-level turbulence kinetic energy (TKE), and (6) emission and uplift of mineral dust in the lee of nearby mountains. The thermally forced meso-γ scale adjustment processes, which occurred in the canyons/small valleys, may have been the cause of numerous observed dust streaks leading to the entry of the dust into the atmosphere due to the presence of significant vertical motion and TKE generation. This study points to the importance of meso-β to meso-γ scale adjustment processes at low atmospheric levels due to an imbalance within the exit region of an upper level jet streak for the formation of severe dust storms. The low level TKE, which is one of the prerequisites to deflate the dust from the surface, cannot be detected with the low resolution data sets; so our results show that a high spatial resolution is required for better representing TKE as a proxy for dust emission.

1. Introduction

There are three pathways of dust transport from North African sources. First, dust is exported across the Atlantic Ocean to the United States, the Caribbean, and South America (Perry et al., 1997; Prospero & Lamb, 2003; Swap et al., 1992); second, dust is transported to the Mediterranean and Europe (Avila & Penuelas, 1999; Borbely-Kiss et al., 2004; Franzen et al., 1994; Moulin et al., 1998); and third, dust is transported toward the eastern Mediterranean and the Middle East (Ganor, 1994; Israelevich et al., 2002; Kubilay et al., 2000; Yaalon & Ganor, 1979). During the northern hemisphere cold season (November to April), the North African climate is influenced by the northeasterly trade winds called the Harmattan, which is the result of meridional pressure gradients at the synoptic scale across the Saharan desert and can be viewed as part of the meridional circulation (Burton et al., 2013). Fiedler et al. (2015) showed that synoptic scale cold air advection over North Africa causes increased intensity and fluctuations in this system, that is, the Harmattan surges. Regionally, the importance of the study of the Harmattan wind system has been increasing since this system advects a significant amount of mineral dust equatorward, causing negative impacts on visibility, agriculture, and human health (e.g., causes meningitis) (Burton et al., 2013; Kalu, 1979; Pérez García-Pando et al., 2014).

The Middle East is also one of the major dust storm regions during the cold season. The dust storm of 10 March 2009, which was not predicted in advance, caused widespread impacts, such as respiratory problems for people in the northeastern, eastern, and central parts of Saudi Arabia and most of Kuwait, covering a distance of about 1,500 km and an area of about 300,000 km^2 (Alharbi et al., 2013). This widespread storm, which lasted several hours and struck Riyadh, was one of the most intense dust storms experienced in Saudi Arabia in the last two decades (Alharbi et al., 2013).

Additionally, the Bodélé Depression in Chad, which occupies an area of 0.5% of the size of the Amazon or 0.2% of the Sahara, located between northeast of Lake Chad (17°N 18°E) and the Tibesti Mountains (Koren et al., 2006; Washington & Todd, 2005) is one of the most active dust storm formation zones in the world. Todd et al. (2007) estimated that during dust storms from the Bodélé, about 1.2 Tg (Teragram) of dust is

emitted per day, which represents between 6 and 18% of the total global dust emission. Besides this, emitted dust from the Bodélé plays an important role in fertilizing the Amazon rain forest (Swap et al., 1992; Todd et al., 2007).

There are many studies about the impacts and transport of Saharan and Middle East dust globally, but there is less research addressing the detailed mesoscale atmospheric processes, which are leading to severe dust storms. To better understand atmospheric processes of dust storms through finer spatial and temporal analyses, three case studies of dust storms have been selected and analyzed in depth. These are as follows: (1) the Harmattan dust storm of 2 March 2004 in North Africa, (2) a Saudi dust storm of 9 March 2009, and (3) a severe Bodélé Depression dust storm of 8 December 2011. As all these three selected dust storms occurred in the lee of the mountains; this study also aims to reveal some commonalities and differences of the generation of a strong low-level wind during the jet adjustment processes, which were responsible for the large-scale dust storms. We make use of rawinsonde soundings, surface observations, and numerical model output for each of the three cases. In this manuscript we first review previous studies on the jet adjustment processes responsible for dust storms outside of North Africa and Saudi Arabia. Based on this review, we transfer this knowledge to North African conditions and outline our hypothesis for regional dust storm genesis in these locations. The next sections describe the methodology and results of the observational analyses as well as added detail from numerical model output in each of these three cases followed by the overall conclusions.

1.1. Review on Jet Adjustment Processes

Past literature on jet adjustment processes causing dust storms focused on the central United States. Lewis et al. (2011) described a paradigm of a transition of a transverse indirect circulation to a direct circulation in the exit region of an upper level jet streak to generate a strong low-level wind and vertical motion for dust deflation and uplift. In this study as well as one on two dust storms occurring over northwestern Nevada Kaplan et al. (2012), it was found that favorable lower tropospheric dust storm dynamics are initiated first aloft (e.g., midtropospheric level) by the breakdown and subsequent imbalance between the geostrophic wind and the total wind in the exit region of the polar jet characterized by relatively high Lagrangian Rossby numbers ($\geq$0.5) in the flow.

Pokharel, Kaplan, and Fiedler (2016) assessed a major dust storm in northwest Africa and found that the development started after the interaction of the exit region of the jet streak with the perturbed air mass in the lee of the mountains. The lower tropospheric mesoscale response to this flow imbalance, namely, the development of mesoscale mass-field adjustments, subsequently occurred, where a direct transverse circulation about the jet generates the ageostrophic/isallobaric winds at low levels (Rochette & Market, 2006) and the coincident development and deepening and destabilization of the planetary boundary layer (PBL). This is consistent with Lewis et al. (2011). A thermal wind imbalance accompanies this process and is caused by the confluence of the polar and subtropical jets, which produces a series of mesoscale circulations during dust storm genesis in many locations including the Southern Plains of the U.S. (Kaplan et al., 2013b). These studies (Kaplan et al., 2012, 2013a, 2013b; Lewis et al., 2011) largely agree on the atmospheric processes for the generation of dust storms in the U.S., that is, the role of tropospheric jets, and a deep PBL with strong turbulence.

1.2. Hypotheses

Our hypothesis follows the aforementioned studies in that ageostrophic motions develop in the jet streak exit region, with a focus on the precursor mountain-induced thermal perturbation/inversion that perturbs the jet and results in thermal wind imbalance. The relevant mountain ranges are here the Atlas Mountains in the Harmattan case, the Sarawat Mountains in the Saudi case, and the Tibesti Mountains in the Bodélé Depression case. The interaction between the jet exit region and terrain-induced thermal perturbation first manifested itself in the lee of the mountains. The leeside mass perturbation, caused by the development and blocking of a leeside inversion due to localized downslope warming, leads to the development of a thermally direct ageostrophic circulation pattern and mesoscale vertical motion when the jet streak exit region approaches a mountain. This thermally direct ageostrophic circulation (developed as a transition of a transverse indirect circulation to a direct circulation) develops in response to the geostrophic imbalance across the exit region of the upper level jet streak over the leeside of the mountains. In the thermally direct circulation, kinetic energy is generated as warm air rises and adiabatically cools on the warm side (right exit), while cold

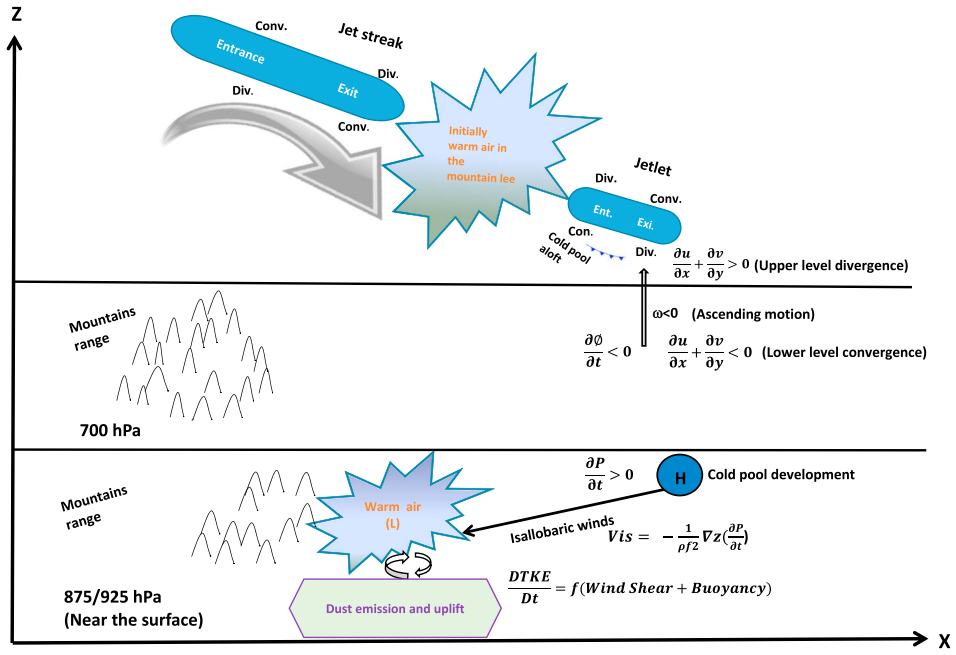

Figure 1. Schematic diagram of imbalance in the exit region of the jet streak and the subsequent jet adjustment processes leading to the dust storms. Regions of horizontal convergence (conv.) and divergence (div.) are marked. Please refer to the conclusion section for a detailed explanation of the identified processes.

air must sink and adiabatically warm on the cold side of the jet (left exit) to complete a circulation to maintain the balance in the exit region of the jet. A high Lagrangian Rossby number is typical in such a weather regime ($R_0 \geq 0.5$), for example, strong Lagrangian accelerations as those observed and simulated in dust storms in the Southwestern U.S. (Kaplan et al., 2011, 2013a, 2014). This hypothesis will be tested and further expand to include the concept that based on this high Rossby number ($R_0 \geq 0.5$) flow environment, a favorable thermodynamic and hydrodynamic state in the PBL is established to create the necessary turbulence kinetic energy (TKE) for dust deflation and uplift (Kaplan et al., 2012; Zhang et al., 2000). All of these processes starting from the interaction of the exit region of the jet streak with the perturbed air mass in the lee of the mountains leading to the occurrence of the dust storm are presented in the schematic diagram (Figure 1). This hypothesized concept of dust storm development in Northern Africa and Saudi Arabia will be tested with three case studies in the following sections of this manuscript.

2. Materials and Methods

For each case, we first examined the following remotely sensed and conventional observational data sources: (1) satellite imagery from the Moderate Resolution Imaging Spectroradiometer (MODIS) (https://ladsweb.nascom.nasa.gov/)/Aqua and Terra (level 1b, collection 5.1, 1 km resolution, and RGB composite), (2) Meteosat-8 animation imagery provided by the European Organisation for the Exploitation of Meteorological Satellites (EUMETSAT) (http://www.eumetsat.int/website/home/Images/ImageLibrary/DAT_IL_04_03_06_F.html) (only available for the Harmattan case), (3) rawinsonde soundings from the University of Wyoming (http://weather.uwyo.edu/upperair/sounding.html) (only available for the Harmattan case and for the Saudi case), and (4) aerosol optical depth imagery captured by the MODIS/Aqua instrument (level 3 daily (D3). Additionally, (5) observational surface data archived by Weather Underground (wunderground.com, e.g., Bechar, Tindouf, Adrar, and Timimoun surface stations in Algeria for the Harmattan case; Adrar, Hafr al-Batin, Hail, Jeddah, Al-Madinah, Makkah, Rafha, Riyadh, and Turaif stations in Saudi Arabia for the Saudi case; and Ndjamena station in Chad for the Bodélé case) were analyzed. These data were supplemented by an aerosol modeling system at 1° × 1° horizontal resolution every 6 h from the Navy Aerosol Analysis and Prediction System (NAAPS) (http://www.nrlmry.navy.mil/aerosol_web/).

Gridded reanalysis obtained from the Modern Era Retrospective-Analysis for Research and Applications (MERRA) (https://disc.sci.gsfc.nasa.gov/mdisc/data-holdings/merra/merra_products_nonjs.shtml; Rinecker

et al., 2011) was used for the synoptic to mesoscale observational atmospheric processes, namely, surface pressure, geopotential height, air temperature, wind speed and direction, vertical motion, vertically integrated atmospheric mass tendency, and kinetic energy tendency due to variations in the pressure gradient force. These data were used to make horizontal cross sections at different pressure levels as well as vertical cross sections of u- and v-wind components and potential temperature at a resolution of 0.50° × 0.67°.

To achieve more detailed spatial and temporal accuracies of the analysis of the atmospheric processes such as time periods of deviations from geostrophic balance and adjustment processes during the occurrence of the dust storms, the Weather Research and Forecasting (WRF) model (Skamarock et al., 2008) was run over the different regions employing National Centers for Environmental Prediction/Global Forecasting System (1° × 1°) products as initialization and lateral boundary conditions.

For all these three cases, the Advanced Research WRF model was initialized over a 54 km horizontal resolution parent domain. Additionally, three domains were nested into the parent domain having 18 km, 6 km, and 2 km resolution in each of these three cases. In each case, the lower resolution domains were initialized earlier than the higher resolution domains to generate initial and lateral boundary conditions that are free of possible artifacts associated with the initialization of the parent domain. Table 1 describes the list of available observational data sets, horizontal grid dimensions, the integration times, and the model physics applied in all three dust storm cases at 18, 6, and 2 km horizontal resolution.

3. Results and Discussion

3.1. Harmattan Dust Storm Case Study (Atlas Mountain Dust Storm Case Study)

3.1.1. Observational Analysis

In order to observe the vertical temperature and wind speed/direction profiles at different pressure levels close to the time period of the interaction of the large scale jet with the Atlas Mountains and prior to the dust storms (Figures 2a–2c), the rawinsonde sounding for Bechar (31.5°N 2.25°W) at 0000 UTC 2 March 2004 in Algeria was employed during 2 March 2004 as can be seen depicted in Figure 3a. As Bechar lies to the east of Atlas Mountain and is the closest sounding station to the Atlas Mountains, we expect that the information regarding vertical profiles of different meteorological variables from Bechar before and after the jet streak/mountain interaction could be well represented in this analysis. Figure 3a shows that there were multiple stratified layers (from surface to ~585 hPa) indicative of the presence of the discontinuous stratification of the atmosphere over this area at that time. Such complex stratification on the leeward side of the Atlas Mountains implies possible disruption of the cross-mountain flow by the barrier consistent with differential sinking and stably stratified layers, that is, blocking of the flow.

In proximity to this observation, station data indicated that there were different scales of dust storms at Tindouf (27.67°N 8.13°W), Bechar (31.66°N 2.27°W, north east of Tindouf), Adrar (27.84°N 0.19°W, east of Tindouf), and Timimoun (29.25°N 0.28°W, east of Tindouf) in Algeria from the late morning on 2 March 2004 onward with strong wind speeds and poor visibility (stations are marked by the red stars in Figure 2a). The image shown by the MODIS images on 2–3 March 2004 illustrates the large-scale imagery of the accumulation of dust from these different scales (when the storm reaches synoptic scales, that really is a result of scale interactions) of dust events beginning from early on 2 March and afterward (Figures 2a–2c). The signal of the dust evolution in and around our region of interest (North West Africa) in NAAPS is also consistent with the surface observations.

The midtropospheric synoptic overview from the MERRA shows that there was a positively tilted trough (oriented along a southwest-northeast axis) in the southern part of Europe (i.e., Spain and Portugal) with an evolving ageostrophic wind indicative of the development of curved flow by the slight change of the wind direction (e.g., initiation of rotation/cyclonic curvature vorticity) near the trough axis at 28°N 1°W–32°N 3°E at 0000 UTC on 2 March 2004 (Figures 4a and 4b). The geopotential height consistently showed a deep cold positively tilted trough with falling heights in time over the Djeifa, Laughout, Bechar, and Taghit of Algeria (north to west part of Algeria). From 0600 UTC 2 March to 1200 UTC 3 March, this deep trough cyclonically rotated to be oriented more northwest-southeast across Algeria (not shown). The jet at 500 hPa was propagating toward the Atlas Mountains from north-northeast of Morocco and with further amplification over time; therefore, it was continuously advancing southeastward, influencing the trough till the time of the dust storm. The baroclinic amplification of the jet streak was consistent with the deepening of the trough at the

Journal of Geophysical Research: Atmospheres

10.1002/2017JD026672

Table 1
List of Observational Data Sets and Horizontal Grid Dimensions, Integration Times, and WRF Model Physics Applied in All Three Dust Storm Cases

Dust storm cases	List of observational data sets	Horizontal grid dimensions (west-east and north-south directions)	Integrated time	WRF model physics
Harmattan dust storm	MODIS and EUMETSAT imageries, radiosonde soundings, aerosol optical depth by MODIS, surface data from Weather Underground, and MERRA data sets	82 × 118 grid points (54 km grid spacing) 208 × 274 grid points (18 km grid spacing) 502 × 613 grid points (6 km grid spacing) 802 × 802 grid points (2 km grid spacing)	1200 UTC 1 March to 1800 UTC 3 March 2004 1800 UTC 1 March to 1800 UTC 3 March 2004 0000 UTC 2 March to 1800 UTC 3 March 2004 1200 UTC 2 March to 1800 UTC 3 March 2004	1. Momentum and heat fluxes at the surface using an Eta surface layer scheme (Janjić, 1996, 2001) that follows Monin-Obukhov similarity theory. 2. Turbulence processes following the Mellor-Yamada- Janjić 1.5 order (level 2.5) turbulence closure model (Janjić, 2001; Mellor & Yamada, 1974). 3. Convective processes following the Betts-Miller-Janjić cumulus scheme (Betts, 1986; Betts & Miller, 1986; Janjic, 1994)- applied only on the 54 and 18 km grid. 4. Cloud microphysical processes following the Thompson double-moment scheme (Thompson et al., 2006; Thompson, Rasmussen, & Manning, 2004), 5. Radiative processes following the rapid radiative transfer model for long wave radiation (Mlawer et al., 1997) and Dudhia's scheme for short wave radiation (Dudhia, 1989). 6. Land-surface processes following the Noah Land Surface Model (Noah LSM) (Chen & Dudhia, 2001; Ek et al., 2003).
Saudi dust storm	MODIS satellite image, radiosonde soundings, surface data from Weather Underground, and MERRA data sets	82 × 97 grid points (54 km grid spacing) 208 × 232 grid points (18 km grid spacing) 502 × 553 grid points (6 km grid spacing) 802 × 760 grid points (2 km grid spacing)	0000 UTC 9 March to 1200 UTC 10 March 2009 0600 UTC 9 March to 1200 UTC 10 March 2009 1200 UTC 9 March to 1200 UTC 10 March 2009 1200 UTC 9 March to 1200 UTC 10 March 2009	
Bodélé dust storm	MODIS image, surface data from Weather Underground, and MERRA data sets	82 × 97 grid points (54 km grid spacing) 208 × 232 grid points (18 km grid spacing) 502 × 553 grid points (6 km grid spacing) 802 × 760 grid points (2 km grid spacing)	0000 UTC 8 December to 1200 UTC 9 December 2011 0600 UTC 8 December to 1200 UTC 9 December 2011 0600 UTC 8 December to 1200 UTC 9 December 2011 0600 UTC 8 December to 1200 UTC 9 December 2011	

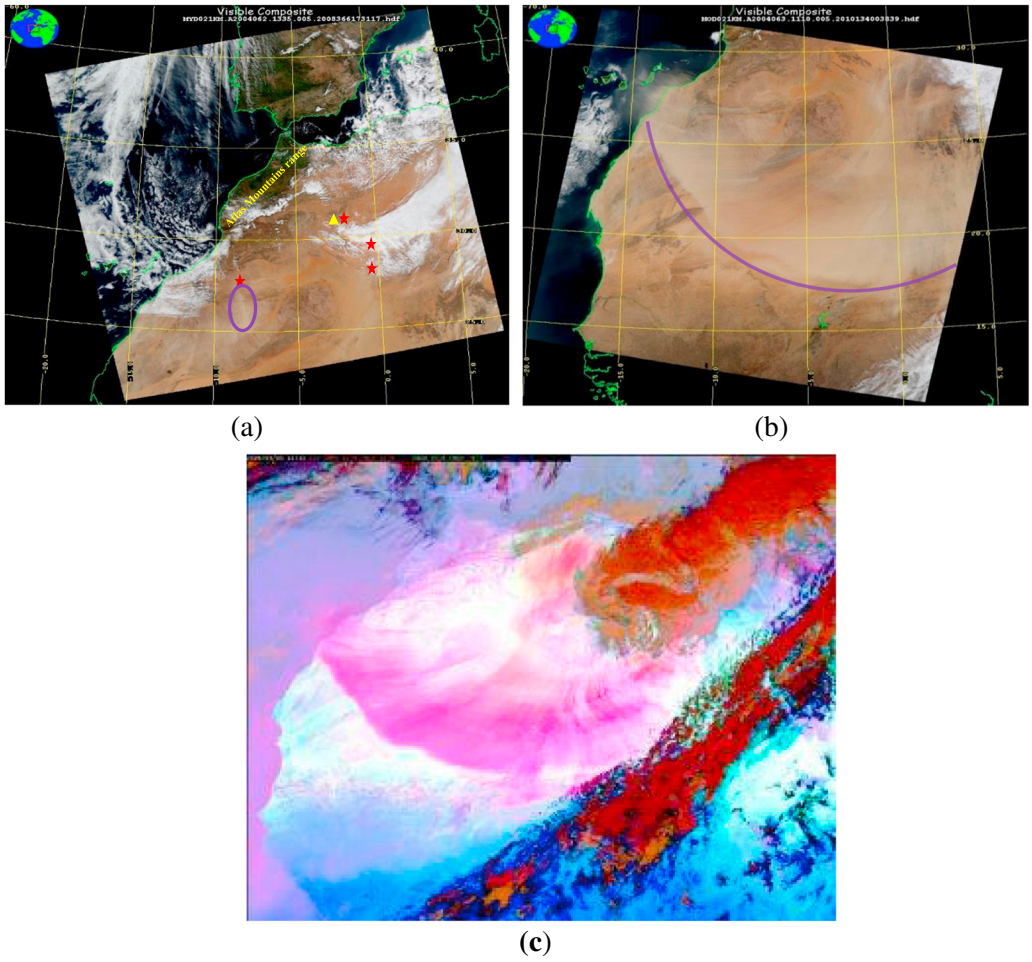

Figure 2. (a) Dust storm image captured by MODIS/AQUA at 1335 UTC on 2 March 2004 (source: https://ladsweb.nascom.nasa.gov). The red stars indicate surface stations (Bechar, Tindouf, Timimoun, and Adrar of which *x* and *y* coordinates are mentioned in section 2) in Algeria, which captured the dust storms on 2 March 2004 (source: wunderground.com). The yellow triangle indicates soundings station at Bechar in Algeria. The purple colored circle shows the area of dust plume. (b) Dust storm image captured by MODIS/AQUA at 1110 UTC on 3 March 2004 (source: https://ladsweb.nascom.nasa.gov). The purple colored arc depicts the outline of the arc of dust plume. (c) Dust storm image captured by Meteosat-8, on 3 March 2004, 1200 UTC, RGB composite. IR12.0–IR10.8, IR10.8–IR8.7, and IR10.8 (source: http://www.eumetsat.int/website/home/Images/ImageLibrary/DAT_IL_04_03_06_F.html). The pink colored arc shows the dust plume.

meso-α/synoptic scale (between 200 km and 2,000 km). Given the location of trough amplification it (exit region of the jet streak) is becoming proximate to the stable layers in Figures 3a and 3b, that is, proximate to mountain-induced thermal perturbation on the lee of the Atlas Mountains resulting in a mass perturbation. This interaction of this perturbed mass ahead of the jet and the exit region of the jet leads to a breakdown of geostrophic balance and will be analyzed with high resolution and time-continuous numerical simulations in this data-sparse region of the Earth.

3.1.2. WRF Simulation Analyses

The analysis of the 18 and 6 km WRF simulation fields over the region depicted in Figure 5 indicates that the exit region of the polar jet streak interacted with a local thermally perturbed air mass on the leeward side of the Atlas Mountains. The presence of the thermally perturbed air mass (inversion sloping down from the mountain toward the Earth's surface) in the lee of the Atlas can be seen by the sinking of isentropic surfaces of the 6 km WRF in the simulated vertical cross sections extending over a north-south axis and located at 30.5–32.5°N along 2°W (not shown). This is also shown by the stable thermal ridge above the deep dry adiabatic lapse rate early in the morning captured by the rawinsonde soundings and the 6 km WRF simulated soundings at Bechar (Figures 3a and 3b). The simulated wind flow strongly suggests that this mass/local thermal perturbation contributed to the generation of an ageostrophic jetlet at 0900 UTC on 2 March 2004 on the lee side of the Atlas over the 30–32°N 6–2°W region (Figure 6), when the jet exit region

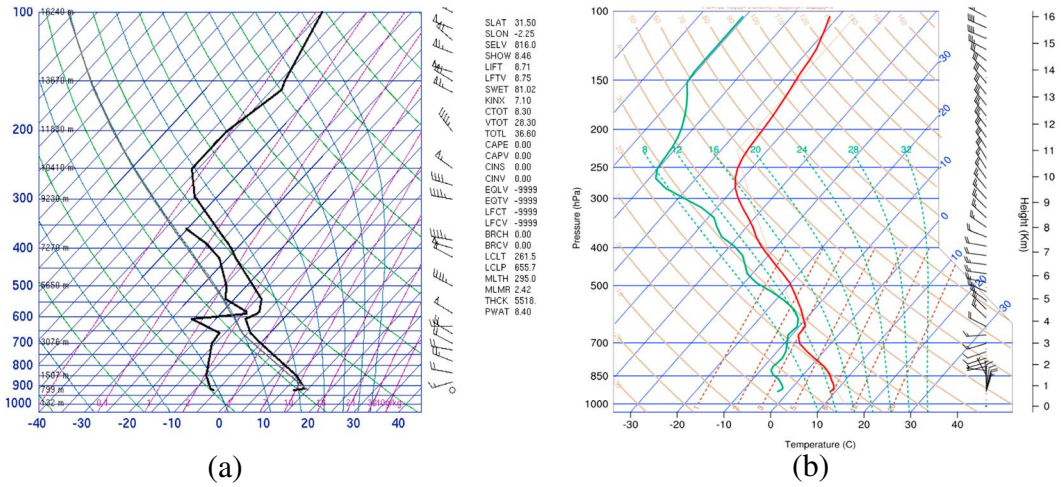

Figure 3. (a) Atmospheric soundings at 0000 UTC 2 March 2004 at Bechar in Algeria (source: University of Wyoming). (b) Atmospheric soundings at 0000 UTC 2 March 2004 at Bechar in Algeria plotted from WRF simulation (6 km resolution).

encountered the perturbed thermal field in the lee of the Atlas Mountains. This mass perturbation accompanying stable stratification is consistent with flow blocking in the lee of the Atlas Mountains based on a subcritical value of the Froude number (Fr $<$ 1) (magnitude of the Froude number indicates the potential for the blocking of the flow) at 32.07°N 2°W, which is 0.83. The Froude number (Smolarkiewicz & Rotunno, 1989) is defined as,

$$\mathrm{Fr} = \frac{U}{NH} \tag{1}$$

where U is the wind speed, N is the Brunt-Väisälä frequency, and H is the height of the mountain. As the momentum advection in the jet exit region encountered the blocked air, it is equivalent to encountering an increasing cross-stream and upstream-directed pressure gradient force (if air parcels with significant kinetic encounter a mass perturbation, their kinetic energy may not be sufficient to overcome the enhanced potential energy consistent with a mass perturbation, so blocking and enhanced potential energy are consistent and equivalent concepts) caused by a mesoscale ridge consistent with a subgeostrophic state, that is, geostrophic wind $>$ total wind. This ridge-induced pressure gradient force deflected and accelerated the wind flow toward the left in a region of the jet at 500 hPa that is typically decelerating if thermal wind balance is to be maintained (see jet streak in schematic depiction in Figure 1), that is, balanced exit region turning to the right of the stream by the larger Coriolis force. This can be seen as a WRF-simulated mesoscale jet or jetlet as the exit region of the large-scale jet streak was deflected by the leeside mass perturbation and accelerations developed consistent with high Rossby number flow not unlike the analogous smoother signal of such a circulation as noted in the MERRA data.

Subsequently, winds were forced to increase above their initial subgeostrophic value in an effort to achieve geostrophic balance. This acceleration forces a mass flux divergence/convergence couplet at 500 hPa and below it (divergence aloft and convergence beneath it), respectively inconsistent with a balanced exit region with divergence equatorward and convergence poleward. In this mass adjustment process, a thermally direct transverse ageostrophic circulation in the exit region of the jetlet developed downstream from the mountains leading to the upward motion and adiabatic expansion resulting in the formation of a cold pool under the right exit of the jetlet (where velocity divergence exists) at 500 hPa (Figure 7). Here an elongated zone of isotherms, a "nose"-like structure, developed indicative of the cooling process caused by adiabatic expansion in response to the mass flux divergence (marked in Figure 7). The development of the cooling is also shown in the WRF simulation with 6 km horizontal resolution at 1400 UTC where the lapse rate increased. This cold pool is associated with a newly generated zone of denser air, which led to the rise of the low-level hydrostatic pressure. Moreover, this mass adjustment aloft included creating an isallobaric-ageostrophic wind (seen after plotting geopotential height contour and wind) near the low-level hydrostatic pressure rises (note equation (2); e.g., Bluestein, 1992; Rochette & Market, 2006),

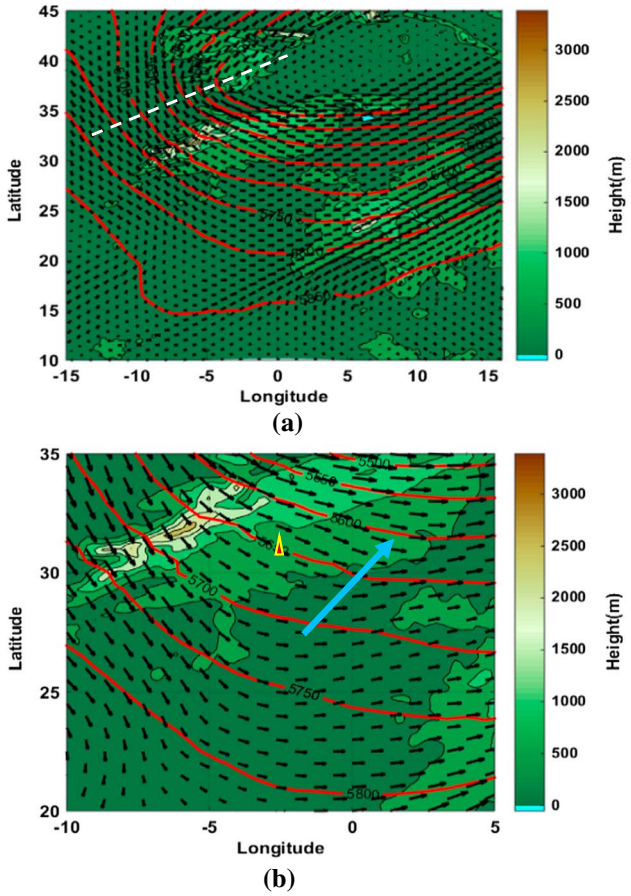

Figure 4. (a) Geopotential height in step of 50 m (red contours), wind speed/direction (small black colored vectors), and the orientation of the trough at the 500 hPa level at 0000 UTC on 2 March 2004 from MERRA reanalysis with horizontal resolution of 54 km (Pokharel, 2016). The shading illustrates the orographic heights in meter. (b) Enlargement of geopotential height in step of 50s m (red contours), wind speed/direction (vectors), and axis of evolving ageostrophic wind (big arrow) at the 500 hPa level at 0000 UTC on 2 March 2004 from MERRA reanalysis with horizontal resolution of 54 km. The shading illustrates the orographic heights in meters. A triangle of red (inside) and yellow (outside) shows the location of Bechar where the soundings were recorded.

$$\mathrm{Vis} = -\left(1/\rho f^2\right)\nabla(\partial p/\partial t) \tag{2}$$

where ρ is the air density, the horizontal gradient in the pressure tendency $\nabla(\partial p/\partial t)$, and f is the Coriolis parameter as a return branch of the direct circulation of the exit region of the jetlet at the lower levels (e.g., 925 hPa). This newly generated circulation represents compensation in response to the adiabatic expansion/cooling of the rising parcels and their accompanying mass flux convergence. This unbalanced return branch circulation at lower levels indicated the adjustment processes for the restoration of the thermal wind balance in the upper level, although it occurs much faster than a balanced jet would adjust during a larger scale indirect circulation in the jet exit region; that is, mass adjusts rather than the wind. This low-level return branch ageostrophic wind accompanying the isallobaric/ageostrophic flow (e.g., meso-β scale adjustment processes) represented a southwestward-directed acceleration, which advected the cold air generated by the ascending flow southwestward roughly parallel to the lee of the Atlas Mountains (upstream and equatorward from the region of the exit region of the jet streak imbalance) by 1500 UTC, where the newly generated deep cold air pool above the surface in the lower-midtroposphere created a dry adiabatic/buoyant lapse rate extending downward from the mid into the lower troposphere.

The consequence of this cooling is to generate decreased static stability in the form of an adiabatic/well-mixed air column as it is heated from below consistent with the strong temperature gradient at the edge of the cold pool at the 850 and 925 hPa levels and the accompanying separation of the isentropic surfaces at lower levels (Figure 8a). The interaction of this accelerating low-level ageostrophic wind with the layer of more buoyant air resulted in a favorable environment for TKE generation (Figure 8b) by buoyant eddies due to the summation of the wind shear and the buoyancy source terms in the TKE time tendency equation (Stull, 2000),

$$\frac{\partial \mathrm{TKE}}{\partial t} = -V.\nabla \mathrm{TKE} + u*^2\left(\frac{\partial \mathrm{u}}{\partial \mathrm{z}}\right) + g\left(\frac{Qs}{Tv}\right) - \varepsilon \tag{3}$$

where $-V.\nabla$TKE is the TKE advection by the mean wind, u^{*2} $(\partial \mathrm{u}/\partial \mathrm{z})$ is generated shear, g (Qs/Tv) is buoyancy, and ε is the dissipation of TKE or eddy dissipation rate. After the generation of significant magnitudes of TKE, there was a low level well-mixed/turbulent eddy circulation that was favorable for ablating dust from the surface and resulted in widespread dust emission. This is consistent with dust storms observed at Adrar, Bechar, and Timimoun and in the NAAPS simulation.

At the same time, besides these meso-β scale adjustment processes discussed so far, there was the development of significant vertical motion, TKE, and vorticity, which persisted in lee of the northeastern parts of Atlas Mountains (~32°N 1.2°W). This development is only visible in the 2 km WRF simulation (Figure 8c), but not in the 6 km simulation that resolved much less of the turbulence in the boundary layer. It is thereby a clear indication of meso-γ scale (between 2 and 20 km) adjustment processes. This small-scale adjustment process occurred when the cold air from the high pressure region of the bottom part of a canyon accompanying the newly formed isallobaric/ageostrophic flow was advected toward and over the thermally forced low pressure area, which formed in the upper parts of the canyon due to the precursor surface sensible heating. This upward flow from canyon to the well-mixed turbulent PBL shows the establishment of thermally direct circulation, which led to the generation of even more concentrated and narrow TKE in the canyon after the reduction of the static stability due to the thermally forced low pressure in the upper parts of the canyon. This led to an establishment of a well-mixed circulation

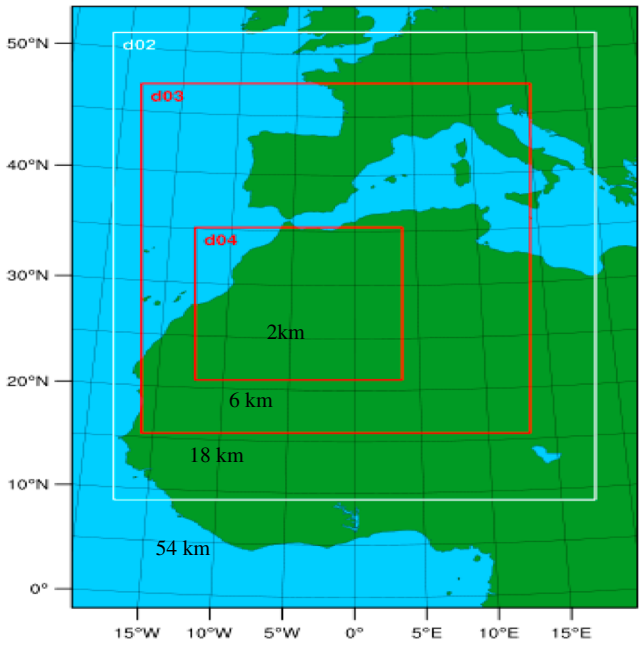

Figure 5. WRF domain configuration for the Harmattan dust storm case in Figures 2a–2c (Pokharel, 2016). do1, do2, do3, and do4 represent domains of 54, 18, 6, and 2 km resolution, respectively.

resulting in several well-defined dust streaks where the heated sides of the canyon became juxtaposed with shearing and colder air above it, which enhanced 3-dimensional rotation as a result of solenoid term in the nonhydrostatic vertical vorticity tendency equation.

3.2. Saudi Dust Storm Case Study

3.2.1. Observational Analysis

Another interesting dust event occurred in Saudi Arabia on 10 March 2009. It was characterized by a dust front propagating equatorward (Figure 9) that is also well-defined like in the case of Northwest Africa. Soundings from two stations, Ha'il (27.43°N 41.68°E) and Al-Madinah (24.55°N 39.70°E) in Saudi Arabia were used for the analysis of vertical profiles of wind speed/direction and temperature prior to the dust storm (Figures 10a and 10b). The Sarawat Mountains extend along the western border of Saudi Arabia, and these two sounding stations are situated just east of the Sarawat Mountains (Figure 9). Therefore, it is likely that information regarding the vertical profiles of temperature and wind speed/direction before and after the interaction of the jet stream with the Sarawat Mountains are well represented by these data. These soundings also show a well-mixed PBL, indicative of the presence of the discontinuous stratification of the atmosphere at each of these stations at that time.

Surface stations in Saudi Arabia also depicted in Figure 9 reported sequential dust storms prior to this large-scale (≥2,000 km) dust event on 10 March 2009, for example, at Arar (30.90°N 41.13°E), Hafr al-Batin (28.33°N 46.12°E), Ha'il (27.43°N 41.68°E), Jeddah (21.70°N 39.18°E), Al-Madinah (24.55°N 39.71°E), Makkah (21.43°N 39.77°E), Rafha (29.63°N 43.48°E), Riyadh (24.65°N 46.64°E), and Turaif (31.69°N 38.73°E) beginning in the early morning of 9 March. The NAAPS model output also reveals that there were multiple occurrences of dust storms from 0000 UTC on 9 March to 0600 UTC on 10 March over Saudi Arabia and its neighboring countries.

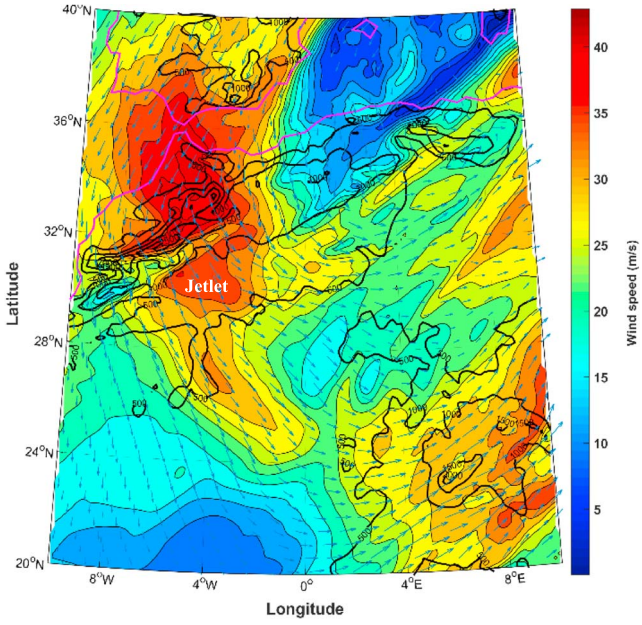

Figure 6. Wind speed (shaded) and direction (vectors) at 500 hPa at 0900 UTC on 2 March 2004 from the midresolution (18 km) (Pokharel, 2016). The black contours show the orographic height in steps of 500 m.

The midtropospheric synoptic overview from the observational MERRA data sets reveals that there was a development of a negatively tilted trough (northwest to southeast oriented axis) and the development of the ageostrophic wind. This is consistent with the development of cyclonic thermal vorticity due to ageostrophic cold air advection within the trough near its axis at 28–29N° 39–41°E (not shown). The negatively tilted trough further deepened until the first occurrence of dust storms. The geopotential height anomaly indicated the consistent deepening of the cold, negatively tilted trough, as falling heights revealed the upper air disturbance over the Middle East and northwestern parts of Saudi Arabia, such as Tabuk, Al Jawf, Sakakah, and Ha'il. From 2200 UTC 9 March to 0900 UTC 10 March the trough propagated southeastward. This propagation of the trough, along with the jet stream, resulted in quasi-geostrophic lifting ahead of the trough and sinking behind it. A jet that was observed at 500 hPa was directed toward the northern edge of Sarawat Mountains moving from the region northwest of Saudi Arabia after 0600 UTC 9 March. This jet was coupled to the trough until the occurrence of the dust storm. Over the course of time, the deepening of the trough at the large scale (between 200 and 2,000 km) was caused by the baroclinic amplification, which was enhanced by this jet. Given the observation of the trough at the location near dust storm genesis, we would expect that several hours before the occurrence of the dust emissions accompanying the dust

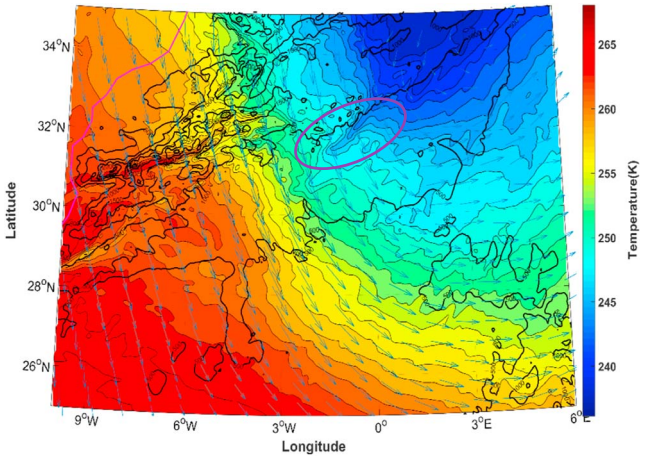

Figure 7. Temperature (shaded) and wind (vectors) at 500 hPa at 1400 UTC on 2 March 2004 from the high-resolution WRF simulation (6 km) (Pokharel, 2016). The circled area marks the cooling area. The black contours mark the orographic height in steps of 500 m.

storm, there was an interaction of the baroclinic wave with terrain oriented southeast to northwest across Saudi Arabia. We use again high-resolution numerical simulations with WRF to study the processes that lead to dust emission and subsequent uplift.

3.2.2. WRF Simulation Analyses

For the study of the detailed jet dynamics proceeding dust storm genesis, the position and the propagation of the jet were analyzed with 18 km and 6 km resolution WRF simulation fields over the region are shown in Figure 11. At 0000–0600 UTC on 9 March 2009 at 500 hPa, a southwest-northeast oriented jet was centered over the northwest of Saudi Arabia (24–28°N 24–32°E), namely designated as J1 and another jet was over the 32–40°N 36–41°E region designated as J2 (Figure 12). At 0600 UTC 9 March, there was the juxtaposition of the entrance region of the J1 at 500 hPa with lower level mesoscale jetlets at 700, 850, 875, and 925 hPa (not shown) indicating a possible coupling between the upper and lower level wind maxima. Evident is a cold pool with an ageostrophic wind component on the southern side of the entrance region of J1 with proximate local ascending motion. The presence of the initial warm pool over a deep layer and the ageostrophic wind on the southern side of the entrance region of J1 was shown by the rise of the geopotential height and acceleration pattern followed by cooling. This early acceleration is an ageostrophic wind that was orthogonal to the geopotential height field, hence an isallobaric-ageostrophic wind component aloft. After the vertical motion accompanying the mass divergence caused by this acceleration resulted in ascent and column cooling, there was the formation of a midtropospheric cold pool that resulted in a compensating low-level height rise at 925 hPa. This cold pool was caused by the upward motion, adiabatic expansion, and local consistent cooling effects of the divergence accompanying the ageostrophic wind aloft.

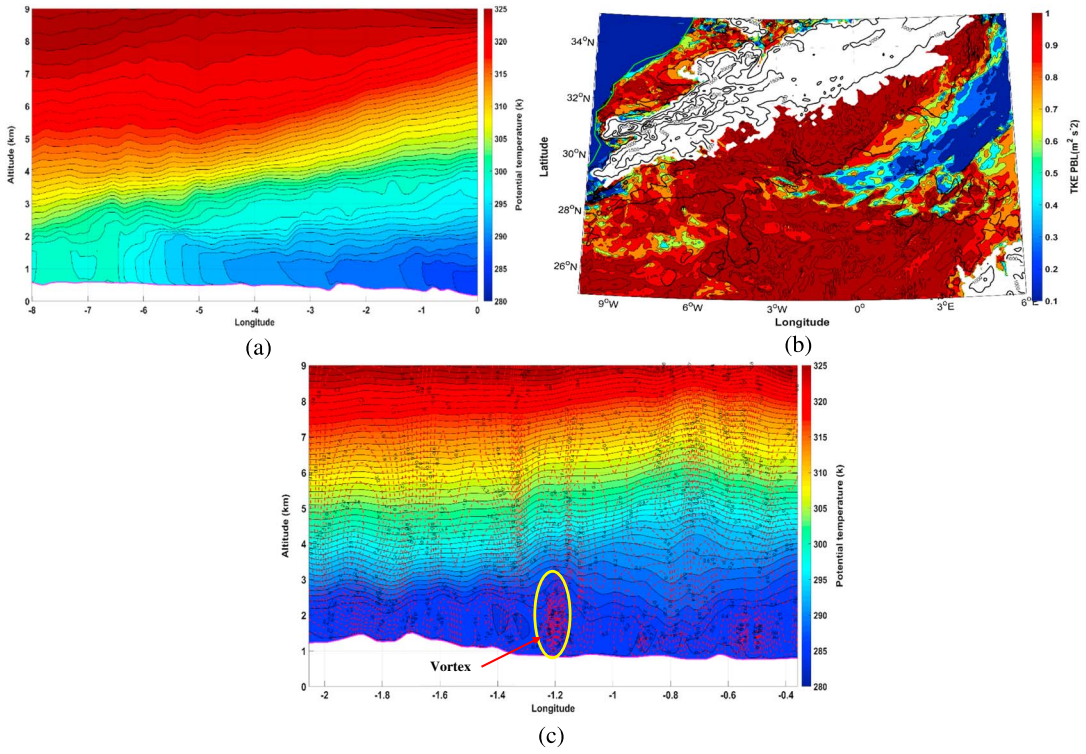

Figure 8. (a) Vertical cross sections of potential temperature at 28.84°N on 1500 UTC 2 March 2004 from the high-resolution WRF (6 km). (b) Turbulent kinetic energy at 925 hPa at 1500 UTC on 2 March 2004 (6 km resolution). (c) Vertical cross sections of potential temperature and w-wind speed components at 32.07°N at 1330 UTC on 2 March 2004 (2 km) (Pokharel, 2016). The circled area marks deep dry convection in the boundary layer.

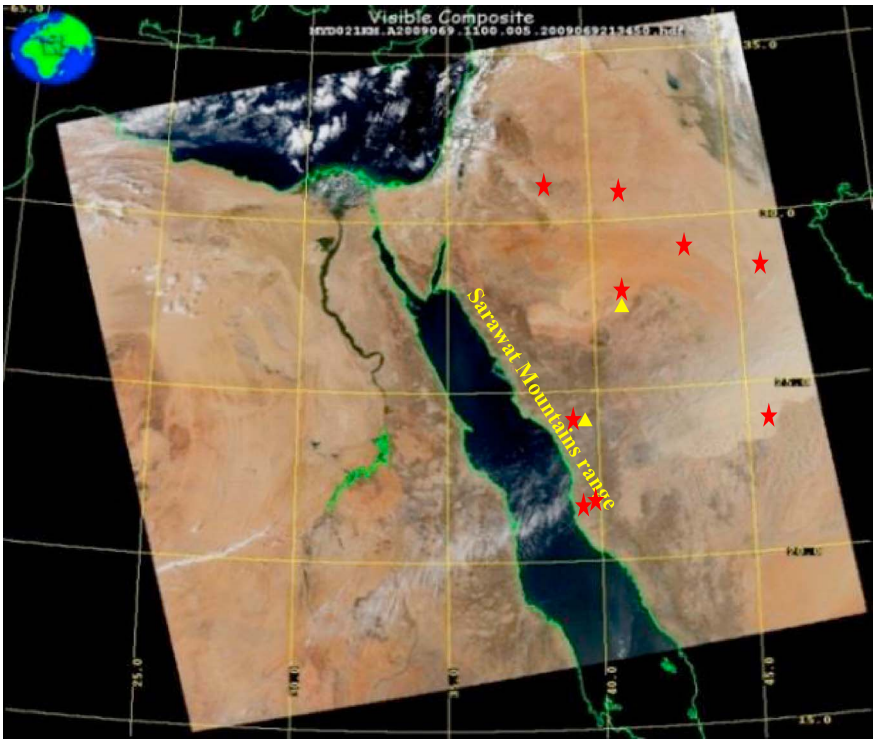

Figure 9. Saudi dust storm image captured by MODIS/Aqua at 1100 UTC on 10 March 2009 (source: https://ladsweb.nascom.nasa.gov). The red stars indicate surface stations (Adrar, Hafr al-Batin, Hail, Jeddah, Al-Madinah, Rafha, and Turaif of which *x* and *y* coordinates are mentioned in section 2) in Saudi Arabia, which captured the dust storms from the early of 9 March 2009 (source: wunderground.com). The yellow triangles indicate soundings stations at Hai'l and Al-Madinah in Saudi Arabia.

The rise of the low-level pressure and the local cooling were seen by the rise of the geopotential height and the decreasing values of potential temperature both of which occurred at 925 hPa. The low-level (925 hPa) height rise created another isallobaric-ageostrophic wind as given in equation (2). This ageostrophic wind was an indication of the return branch of the direct transverse circulation of the entrance region of the J1, thus establishing the low-level jetlet. The return branch ageostrophic wind flow was a westerly/northwesterly wind, which advected the cold air, generated by the ascending flow as mentioned earlier.

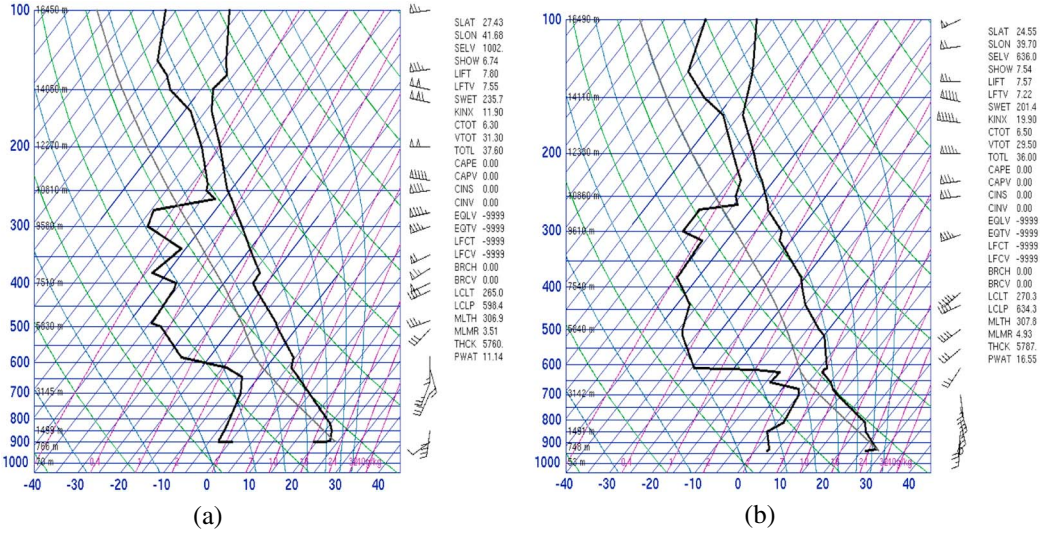

Figure 10. (a) Atmospheric soundings over Hai'l in Saudi Arabia at 0000 UTC on 9 March 2009 (source: University of Wyoming). (b) Atmospheric soundings over Al-Madinah in Saudi Arabia at 0000 UTC on 9 March 2009 (source: University of Wyoming).

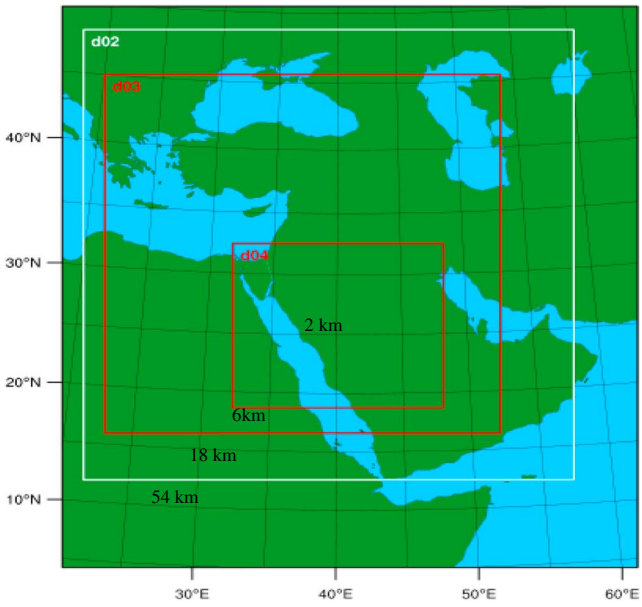

Figure 11. WRF domain configuration for the Saudi dust storm case shown in Figure 9 (Pokharel, 2016). do1, do2, do3, and do4 represent domains of 54, 18, 6, and 2 km resolution, respectively.

After encountering the mountains in Egypt (26–27°N 32–33°E), which lies on the northwest border of the Red Sea, this westerly/northwesterly wind was deflected as northerly/northeasterly wind over the 12–20°N 24–36°E region, where the warm buoyant air mass was present well before the previous adjustments. This deflection represents blocking flow around these steep mountains. This precursor warm air mass was due to the residual well-mixed air mass of the previous afternoon, which was compressed adiabatically downslope overnight on the lee of the Jebel Is Mountains in Sudan. The presence of the warm air mass is shown by the strong temperature gradient at the edge of the cold pool at 850 and 925 hPa levels over that region and the expansion of isentropic surfaces at lower levels over that region. The interaction of northerly/northeasterly winds with this warm air column resulted in a favorable condition for the generation of TKE as cool air was advected over the well-heated low-level air. The generation of turbulent eddies resulted from the summation of the wind shear and the buoyancy source terms in the TKE time tendency equation (3). Consistent with the production of the significant magnitude of TKE (Figure 13a), there was a well-mixed circulation composed of turbulent eddies (not shown), which could emit dust from the surface of the 16–20°N 24–33°E region at 0600 UTC and afterward on 9 March. This is similar in location and time to the NAAPS results presented earlier. At this time, the 10 m wind ranged from 8 to 13 m/s over this region in the 6 km WRF simulation. Such wind speeds are typical for dust emission, and the deep dry convection efficiently mixes the particles upward.

At the same time of J1 development, there was also the juxtaposition of the entrance region of J2 at 500 hPa with lower level jetlets at 700, 850, and 875 hPa. Like for J1, a low-level cold pool formed to the southeast side of the J2 leading to the development of the ageostrophic/isallobaric winds. This subsequently established a compensating cold pool and low level pressure rise followed by the isallobaric-ageostrophic wind (seen from the plots of geopotential height contour and wind) at 875 hPa. This isallobaric-ageostrophic wind is northwesterly; therefore, it indicates the return branch of the direct transverse circulation of the entrance region of J2, which subsequently advected cold air generated by the upward motion and adiabatic expansion above the warm surface. Consequently, the interaction of this cold air at 875 hPa with the highly buoyant air underneath at 28–33°N, 42–47°E resulted in the production of TKE due to the summation of the wind shear and the buoyancy as defined in equation (3) and caused conditions favorable for the dust storm over the eastern/northeastern region of Saudi Arabia. This is in proximity to observed dust storms compiled by Weather Underground at Rafha and Hafr al-Batin and simulated by NAAPS (not shown).

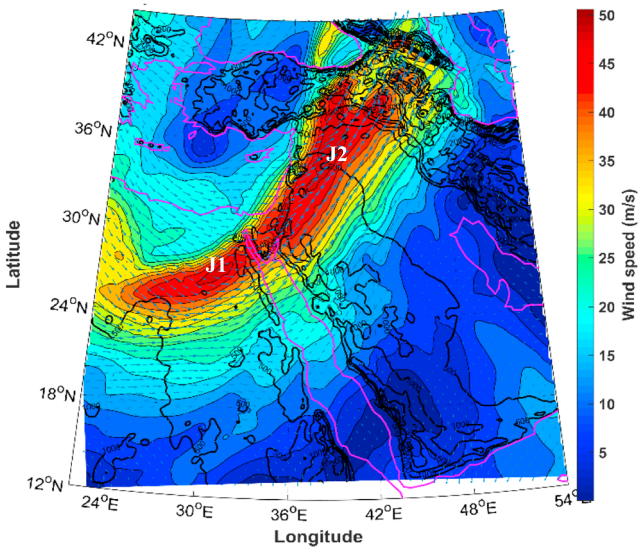

Figure 12. Wind speed/direction at 500 hPa at 0600 UTC on 9 March 2009 (18 km resolution) (Pokharel, 2016). The black contours show orographic height in steps of 500 m.

Like the Harmattan case study above, the blocking of the flow by the complex terrain was also consistent with the low value of the Froude number as given in the equation (1) at 26.7°N 37°E, which is 0.34 ($Fr < 1$) for the discontinuous stratification condition of the air column. The blocking of the flow was facilitated by the presence of the warm stable/thermal ridge above the mixed layer, which was evident in soundings at Hai'l and Al-Madinah in Figures 10a and 10b and vertical cross sections of WRF output along a west-east axis. This thermally modified air mass provided the mass perturbation that generated an ageostrophic jetlet (mesoscale ageostrophic wind) over the 27–28°N 36–38°E region at 0900 UTC 9 March (not shown). This caused the thermal wind imbalance in the exit region of the J1. This imbalance was the result of the precursor Sarawat Mountains' temperature perturbation due to adiabatic compression associated with prejet cross mountain flow. This created a difference between the

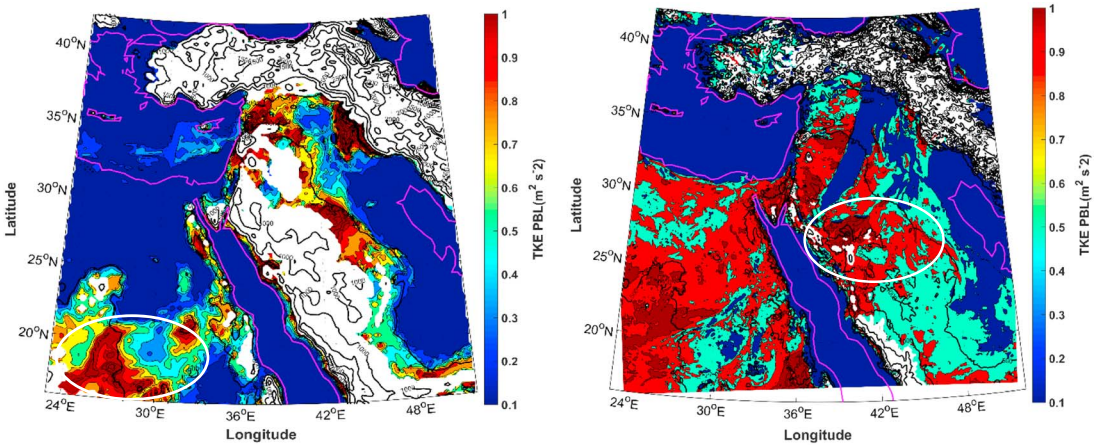

Figure 13. (a) Turbulent kinetic energy at 925 hPa on 0700 UTC 9 March 2009 (18 km resolution). (b) Turbulent kinetic energy at 875 hPa on 1300 UTC 9 March 2009 (6 km resolution).

thermal wind shear (thermal wind shear is the component of shear that is in geostrophic and hydrostatic balance with the temperature field) and the total wind shear necessitating accelerating flow in the exit region of J1 to achieve subsequent thermal wind balance. The leeside warm air mass in two different thermal wind imbalance cases for J1 resulted from precursor advection of the residual PBL of the previous afternoon above the nearby elevated terrain and its subsequent downslope compression adiabatically. The presence of this warm air mass in the lee of the Sarawat was shown by the deep dry adiabatic lapse rate from the soundings at Hai'l and Al-Madinah in Saudi Arabia (Figures 10a and 10b). The presence of the warm air was also supported by the strong temperature gradient at the edge of the cold pool at 850 and 875 hPa levels over that region. After the generation of the aforesaid ageostrophic jetlet due to the imbalance of the exit region of the J1 at 0900 UTC of 9 March, like the adjustment processes discussed in the Harmattan case above, the cold pool formed aloft from the cooling of ascending air mass leading to the ageostrophic isallobaric winds. This subsequently established compensating low level pressure rises leading to generation of another ageostrophic isallobaric wind, which was a northwesterly wind at 875 hPa directed toward south/southeast in the lee of the Sarawat Mountains. This low level ageostrophic isallobaric wind flow advected the cold air generated by the ascending flow toward the warmer air column over the 24–28°N 39–47°E region after 0900 UTC. This process resulted in the generation of TKE (Figure 13b) as defined in the TKE time tendency equation (3) and favored for the occurrence of the dust storms over that region.

3.3. Bodélé Depression Dust Storm Case Study

3.3.1. Observational Analysis

The commonalities of the Northwest African and Saudi Arabian dust storms discussed so far and the literature on U.S. dust storms suggest that there is an underlying physical principle of synoptic-scale dust storms at mountain ranges. To further test this hypothesis, we choose here another dust storm that occurred in the Bodélé Depression downstream of the Tibesti and Ennedi Mountains on 9 December 2011 (Figure 14). Though there were some observational stations in Chad, only one station, which is Ndjamena (12.13°N 15°E) (southwest from the Bodélé Depression) (Figure 14), recorded dust storms from 0600 UTC on 8 to 9 December 2011. At 0600 UTC on 8 December 2011, NAAPS shows the first signal of the dust in the regions west/southwestward and equatorward of the Tibesti Mountains. Six hours later (1200 UTC) the strength and, over time, the areal extension of the dust increased and became concentrated mainly in the southwest of the Tibesti Mountain.

The analysis of midtropospheric atmospheric flow observed from the MERRA data sets shows the development of a positively tilted trough (northeast to southwest oriented axis) and the development of the ageostrophic wind consistent with the initiation of the cyclonic vorticity near the trough axis at 19–20°N 17–19°E at 0600 UTC on 8 December (not shown). The positively tilted trough slightly deepened until the occurrence of dust emission. Although the strength of the positively tilted trough was weak compared to the other cases,

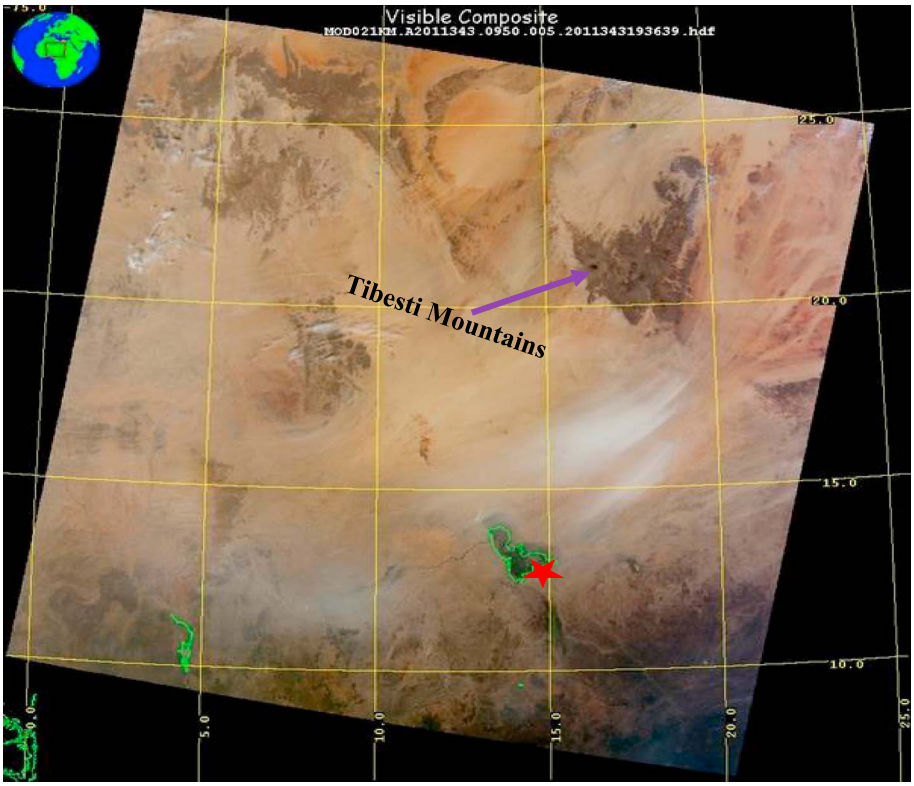

Figure 14. Bodélé Depression dust storm image captured by MODIS/Terra at 0950 UTC on 9 December 2011(source: https://ladsweb.nascom.nasa.gov). The red star indicates surface station at Ndjamena in Chad, which captured the dust storms from 0600 UTC on 8–9 December 2011. The *x* and *y* coordinates of this station are mentioned in section 2.

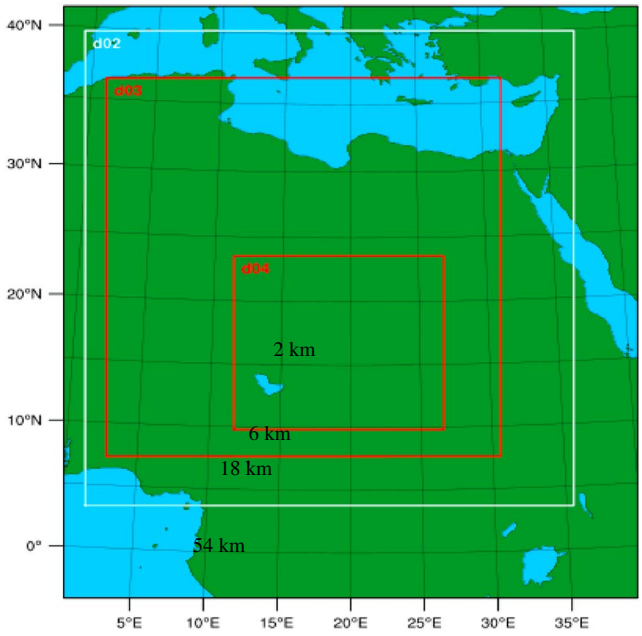

Figure 15. WRF domain configuration for the Bodélé Depression dust storm case shown in Figure 14 (Pokharel, 2016). do1, do2, do3, and do4 represent domains of 54, 18, 6, and 2 km resolution, respectively.

falling heights still revealed the upper-air disturbance over the northeast region of Niger, north and northwestern regions of Chad which included Aozou, and southeast of Libya. From 0900 UTC 8 December to 0900 UTC 9 December this trough propagated southeastward and this propagation of the trough along with the jet stream were both associated with quasi-geostrophic lifting ahead of the trough and sinking behind it. A jet at 500 hPa was over the Tibesti Mountains and additional two jets were north of Chad from 0000 UTC 8 December. The jet, which was over the Tibesti, was coupled to the trough until the occurrence of the dust storm. We again use high-resolution WRF simulations to analyze the dynamical development of the storm.

3.3.2. WRF Simulation Analyses

The position and the propagation of the jet in this case study were analyzed with the WRF simulations with a horizontal resolution of 18 km and 6 km over the region depicted in Figure 15. At 500 hPa there were three jets to be designated as PJ1, PJ2, and STJ3 hereafter over the 30–36°N 25–30°E, 33–36°N 18–24°E, and 20–25°N 18–30°E regions, respectively. PJ1 and PJ2 were oriented northwest-southeast, and STJ3 was oriented along a southwest-northeast axis at 0600 UTC on 8 December 2011, respectively (Figure 16). Over time PJ1 and PJ2 propagated southeastward and STJ3 northeastward. PJ1 and PJ2, which had stronger wind fields, were polar jets because their strong wind signals were not seen above the 200 hPa level, but they were

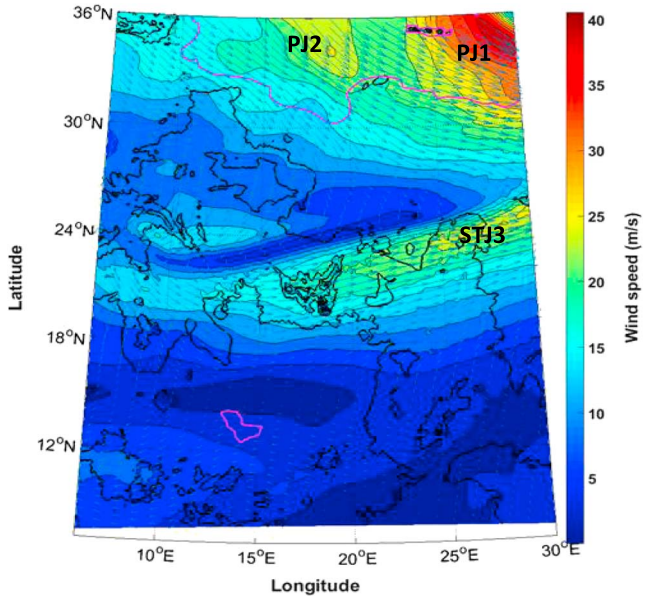

Figure 16. Wind speed/direction at 500 hPa on 0600 UTC 8 December 2011 (6 km resolution).

coupled with lower levels, that is, below 700 hPa, and the synoptic scale winds were maxima due to the presence of the deep cold air mass from higher latitudes sustaining deep thermal wind forcing. On the other hand, STJ3, which was a subtropical jet because the strong wind signal of it was clearly seen far above the 200 hPa level, is as high as 100 hPa but had a weaker midlower tropospheric wind field due to the lack of a supporting low-level cold air mass at lower latitudes, so STJ3 was not seen at lower levels (e.g., below 700 hPa) (Riehl et al., 1954). This shows that PJ1 and PJ2 differed from STJ3 in terms of the strength of each jet versus altitude with STJ3 stronger very high aloft and the opposite for PJ1 and PJ2 (Defant & Taba, 1957).

At the same time (0600 UTC on 8 December 2011) there was a thermal perturbation on the leeward side of the Tibesti Mountains. The presence of the thermal perturbation (inversion sloping down from the mountain toward the Earth's surface) in the lee of the Tibesti is shown by the downward-folded isentropic surfaces (not shown). Based on the position and the time of STJ3 and the perturbation of the u-wind speed components in the region adjacent to the Tibesti Mountains (19.78°N 17.75–18°E) at 0600 UTC, it can be inferred that there was an interaction of the exit region of STJ3 with the perturbed warm air mass on the leeward side (south/southwest/southeast) of the Tibesti Mountains. This interaction was established by blocking of the flow, evident by a low Froude number as given by the equation (1), which is 0.15 at 19.78°N 18.5°E based on the likely baroclinic state (discontinuous vertical stratification). This blocking interaction with the jet exit region resulted in accelerating flow manifested as a jetlet (a wind maximum at the mesoscale) on the leeward side of the Tibesti Mountains. This thermal perturbation created the thermal wind imbalance in the exit region of the STJ3 by making a difference between the thermal wind shear and the total wind shear as a result of accelerating flow in the exit region of the STJ3.

There was also cold pool formation aloft (midtropospheric level) as a result of the generation of the divergent ageostrophic wind and its subsequent local unbalanced ascending flow after the imbalance in the exit region of STJ3. The development of the midtropospheric cold pool favored the generation of the buoyant environment in the lower tropospheric layers. The development of the cooling was also shown by the WRF soundings at 6 km horizontal resolution at 0900 UTC. This acceleration and the cold pool initially aloft (midtropospheric level) represented an ageostrophic wind response orthogonal to the geopotential height field (i.e., unbalanced ageostrophic wind in the subgeostrophic region). To compensate for this midtropospheric level mass flux divergence, ascending adiabatically cooled air and its accompanying mass flux convergence accompanied the cooling and the lower-level tropospheric height rises as noted at 925 hPa at 1200 UTC. The lower-level tropospheric height rise at 925 hPa was generated after the formation of the cold pool from the upward motion, adiabatic expansion, and the local cooling shown by the perturbation of the geopotential height and lower values of potential temperature at 925 hPa. This low-level pressure rise generated the ageostrophic isallobaric wind (note equation (2)) at 925 hPa (seen by the plot of geopotential height contour and the wind), which advected cold air toward the south/southwestward of the Tibesti Mountains (Figure 17), indicative of the unbalanced return branch of the direct transverse circulations of the jetlet. This return branch circulation in the lower level indicated the meso-β scale adjustment processes for the restoration of the thermal wind balance in the upper level. It is to be noted here that, though we see the formation of the lower level ageostrophic isallobaric wind flow as a result of the divergence aloft, we cannot also ignore the possibility of the gap flow between the Tibesti

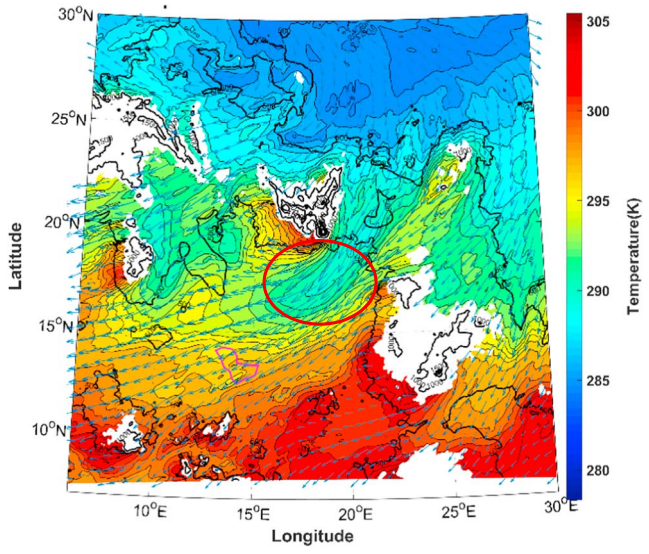

Figure 17. Temperature/wind speed direction at 925 hPa at 1200 UTC on 8 December 2011 from the high-resolution WRF simulation (6 km). The circled area marks cold air advection toward the south/southwestward of the Tibesti. The areas are masked out where 925 hPa lies below the orography. Lake Chad is marked by a pink contour.

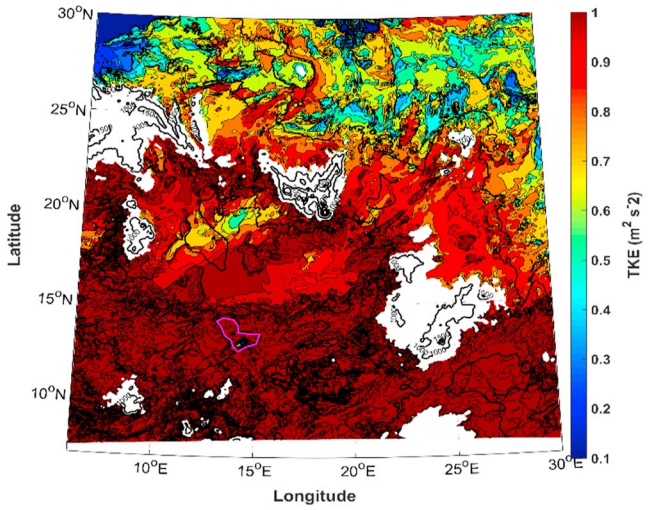

Figure 18. Turbulent kinetic energy at 925 hPa at 1200 UTC on 8 December 2011 (6 km resolution).

and Ennedi Mountains (e.g., Todd et al., 2008; Washington et al., 2006; Washington & Todd, 2005) during that time. This isallobaric/ageostrophic wind interacted with the warm air column formed from the residual air mass of the previous afternoon and its subsequent adiabatic compression downslope on the west/southwest side of the Tibesti Mountains. The presence of the precursor warm air column was shown by the strong temperature gradient at 850 and 925 hPa over that region and the expansion of isentropic surfaces at lower levels over the 15–20°N 15–21°E region. Hence, the overrunning of this ageostrophic cold air above the warm air column resulted in destabilization and a favorable environment for the generation of the significant magnitudes of the TKE (Figure 18). This TKE was due to the effects of the wind shear and the buoyancy terms defined in the TKE tendency equation (note equation (3)). This TKE resulted in a well-mixed circulation and ablated the dust from the Bode'le´ Depression.

In the meantime, besides this meso-β scale adjustment processes, significant vertical motion, TKE, and vorticity, and their persistence over a wide region (19.98°N 17.25–19.5°E) were shown by the 2 km resolution WRF products after the interaction of the exit region of the subtropical jet streak with the thermal ridge. This is an indication of the meso-γ scale adjustment processes. This small-scale adjustment occurred when the cold surge accompanying the newly formed ageostrophic-isallobaric flow from the bottom part of the canyon at the Bode'le´ Depression propagated toward the upper parts of precursor thermally forced (differential surface heating) circulation in the canyon. This precursor upslope and thermally direct flow is from the interior canyon to the well-mixed turbulent planetary boundary layer, which led to the even more concentrated turbulence due to the thermally forced low pressure and accelerating flow in the upper parts of the canyon. These adjustments led to a well-mixed circulation resulting in a dust streak where the heated sides of the canyon paired with shearing and colder air above it increased rotation as a result of 3-dimensional solenoid term in the nonhydrostatic vertical vorticity equation (Bluestein, 1992). As this depressed region occupies a number of small canyons, a large number of dust streaks were generated from the multiple meso-γ scale adjustment processes at that time period, resulting in a widespread plume of dust emission from this region. These dust streaks are clearly seen in MODIS/Terra image (Figure 14).

4. Conclusions

In this study, WRF output replicated similar patterns to the surface and upper-air observational data sets, indicative of the validity of the model. In each of these three subtropical dust storm cases, there was a thermal wind imbalance in the exit region of the midtropospheric jet streak after interacting with the perturbed air mass in the lee of the mountain. This imbalance, or adjustment of the mass field in the form of unbalanced wind velocity accelerations, led to additional mesoscale adjustment processes including the following: (1) the development of a thermally direct circulation in the exit region of the jet and entrance region of the accelerated jetlet, (2) subsequent formation of the cold pool aloft due to the ascending motion-induced adiabatic cooling, and (3) the associated perturbation in the low-level mass field led to the development of the ageostrophic/isallobaric winds at the lower levels. Following the compensating acceleration of the low-level flow, (4) the low-level ageostrophic/isallobaric wind and its colder air was advected above the warm buoyant near-surface air column resulting in the significant magnitudes of (5) buoyancy and shear-induced TKE leading to a well-mixed circulation, which caused widespread, meso-β to meso-α scale dust storms. This shows that our study is consistent with the roles of jet streaks to cause dust storms in North America shown by Kaplan et al. (2012) and Lewis et al. (2011). Besides the roles of jet streaks in the genesis of dust storms, unique to this Bodélé case study is the fact that the subtropical jet streak caused the dust storm unusually close to the equatorial region after its interaction with the thermally perturbed air mass on the lee of the Tibesti Mountains. In the previous two case studies, that is, Harmattan and Saudi Arabian, the polar jet streaks played this same role at higher latitudes.

As this study is a purely atmospheric dynamical study our main goal was to simulate the processes of generation of the strong wind speed at the lower level and the positive buoyancy environment, which are mainly

responsible for the large-scale dust emission and verify these results with higher resolution observations. This is accomplished clearly by the WRF high resolution simulation as well as discussed in the above. Similarly, we were not concerned with quantifying the emission of the dust from the surface to reveal the proof of the dust emission or changes of the dust concentration in the atmosphere before and after the dust storms since this large-scale dust emission was clearly shown by the satellites and other kinds of observations. It is important to note that, in this study, the high-resolution modeling work indicates that turbulence inferred from simulated TKE is a key factor in generating the dust-emitting winds. Turbulence cannot be seen by coarse resolution data, such that dust emission associated with convective buoyancy and accelerating low-level flows would be missed.

Acknowledgments
We would like to thank K.C. King, Robert David, Stephen Noble, Farnaz Hosseinpour, and Kacie Shourd for their help in collecting the observational data sets and running the WRF model. We would also like to thank the National Science Foundation (NSF) and the National Center for Atmospheric Research (NCAR) for providing computational support. We would also like to thank the reviewers (Ron Miller and anonymous reviewer) and the editor, Minghua Zhang, for their insightful comments and suggestions. This work is not funded by any government or private agency. The Division of Atmospheric Sciences of the Desert Research Institute under the direction of Marc Pitchford funded the publication of this research. We would like to state that data used here from the external sources are from cited references. The authors declare that there are no any conflicts of interest.

References

Alharbi, B. H., Maghrabi, A., & Tapper, N. (2013). The March 2009 dust event in Saudi Arabia—precursor and supportive environment. *Bulletin of the American Meteorological Society*, *94*(4), 515–528. https://doi.org/10.1175/bams-d-11-00118.1

Avila, A., & Penuelas, J. (1999). Increasing frequency of Saharan rains over northeastern Spain and its ecological consequences. *Science of the Total Environment*, *228*(2-3), 153–156. https://doi.org/10.1016/s0048-9697(99)00041-8

Betts, A. K. (1986). A new convective adjustment scheme.1. Observational and theoretical basis. *Quarterly Journal of the Royal Meteorological Society*, *112*(473), 677–691. https://doi.org/10.1256/smsqj.47306

Betts, A. K., & Miller, M. J. (1986). A new convective adjustment scheme. 2 single column tests using GATE Wave, Bomex, Atex, and Arctic air-mass data sets. *Quarterly Journal of the Royal Meteorological Society*, *112*(473), 693–709. https://doi.org/10.1002/qj.49711247308

Bluestein, H. B. (1992). *Synoptic-dynamic meteorology in midlatitudes. Volume I: Principles of kinematics and dynamics* (p. 448). Oxford, New York: Oxford University Press.

Borbely-Kiss, I., Kiss, A. Z., Koltay, E., Szabo, G., & Bozo, L. (2004). Saharan dust episodes in Hungarian aerosol: Elemental signatures and transport trajectories. *Journal of Aerosol Science*, *35*(10), 1205–1224. https://doi.org/10.1016/j.jaerosci.2004.05.001

Burton, R. R., Devine, G. M., Parker, D. J., Chazette, P., Dixon, N., Flamant, C., & Haywood, J. M. (2013). The Harmattan over West Africa: Nocturnal structure and frontogenesis. *Quarterly Journal of the Royal Meteorological Society*, *139*(674), 1364–1373. https://doi.org/10.1002/qj.2036

Chen, F., & Dudhia, J. (2001). Coupling an advanced land surface-hydrology model with the Penn State-NCAR MM5 modeling system. Part I: Model implementation and sensitivity. *Monthly Weather Review*, *129*(4), 569–585. https://doi.org/10.1175/1520-0493(2001)129%3C0569:caalsh%3E2.0.co;2

Defant, F., & Taba, H. (1957). The threefold structure of the atmosphere and the characteristics of the tropopause. *Tellus*, *9*, 259–274.

Dudhia, J. (1989). Numerical study of convection observed during the winter monsoon experiment using a mesoscale two dimensional model. *Journal of the Atmospheric Sciences*, *46*(20), 3077–3107. https://doi.org/10.1175/1520-0469(1989)046%3C3077:nsocod%3E2.0.co;2

Ek, M. B., Mitchell, K. E., Lin, Y., Rogers, E., Grunmann, P., Koren, V., … Tarpley, J. D. (2003). Implementation of Noah Land Surface Model advances in the National Centers for Environmental Prediction operational mesoscale Eta model. *Journal of Geophysical Research*, *108*(D22), 8851. https://doi.org/10.1029/2002JD003296

Fiedler, S., Kaplan, M. L., & Knippertz, P. (2015). Supporting information for the importance of Harmattan surges for the emission of North African dust aerosol. *Geophysical Research Letters*, *42*, 9495–9504. https://doi.org/10.1002/2015GL065925

Franzen, L. G., Mattson, J. O., & Martensson, U. (1994). Yellow snow over the Alps and sub-arctic from dust storm in Africa, March 1991. *Ambio*, *23*, 233–235.

Ganor, E. (1994). The frequency of Saharan dust episodes over Tel-Aviv, Israel. *Atmospheric Environment*, *28*(17), 2867–2871. https://doi.org/10.1016/1352-2310(94)90087-6

Israelevich, P. L., Levin, Z., Joseph, J. H., & Ganor, E. (2002). Desert aerosol transport in the Mediterranean region as inferred from the TOMS aerosol index. *Journal of Geophysical Research*, *107*(D21), 4572. https://doi.org/10.1029/2001JD002011

Janjic, Z. I. (1994). The step-mountain Eta coordinate model-further developments of the convection, viscous sub-layer, and turbulence closure schemes. *Monthly Weather Review*, *122*(5), 927–945. https://doi.org/10.1175/1520-0493(1994)122%3C0927:tsmecm%3E2.0.co;2

Janjić, Z. I. (1996). The surface layer in the NCEP Eta model. In *Preprints, 11th Conference on Numerical Weather Prediction* (pp. 354–355). Norfolk, Va: American Meteorological Society.

Janjić, Z. I. (2001). Nonsingular implementation of the Mellor-Yamada level 2.5 scheme in the NCEP Meso model, NCEP Off. Note 437, pp. 61.

Kalu, A. E. (1979). The African dust plume: Its characteristics and propagation across West Africa in winter. In C. Morales (Ed.), *Saharan dust: Mobilization, transport and deposition* (pp. 95–118). Chichester, UK: John Wiley.

Kaplan, M. L., Vellore, R. K., Lewis, J. M., Underwood, S. J., Pauley, P. M., Martin, J. E., & Krishnan, R. (2013a). Re-examination of the I-5 dust storm. *Journal of Geophysical Research: Atmospheres*, *118*, 627–642. https://doi.org/10.1002/jgrd.50131

Kaplan, M. L., Vellore, R. K., Lewis, J. M., Underwood, S. J., Pauley, P. M., Martin, J. E., … Krishnan, R. (2013b). Subtropical-polar jet interactions in Southern Plains dust storms. *Journal of Geophysical Research: Atmospheres*, *118*, 12,893–12,914. https://doi.org/10.1002/2013JD020345

Kaplan, M. L., Vellore, R., Lewis, J. M., Underwood, J., Pauley, P., Martin, J., … Krishnan, R. (2014). Dust storm organization in large Rossby number flows, *ProScience*, *1*, 26–31. https://doi.org/10.14644/dust.2014.005

Kaplan, M. L., Vellore, R. K., Lewis, J. M., & Young, M. (2011). The role of unbalanced mesoscale circulations in dust storms. *Journal of Geophysical Research*, *116*, D23101. https://doi.org/10.1029/2011JD016218

Kaplan, M. L., Vellore, R. K., Marzette, P. J., & Lewis, J. M. (2012). Upstream midtropospheric circulations enabling leeside (spillover) precipitation over the Sierra Nevada? Leeside adjustments to upslope diabatic heating. *Journal of Hydrometeorology*, *13*, 1372–1394.

Koren, I., Kaufman, Y. J., Washington, R., Todd, M. C., Rudich, Y., Martins, J. V., & Rosenfeld, D. (2006). The Bode'le´ Depression: A single spot in the Sahara that provides most of the mineral dust to the Amazon forest. *Environmental Research Letters*, *1*(1), 014005. https://doi.org/10.1088/1748-9326/1/1/014005

Kubilay, N., Nickovic, S., Moulin, C., & Dulac, F. (2000). An illustration of the transport and deposition of mineral dust onto the eastern Mediterranean. *Atmospheric Environment*, *34*(8), 1293–1303. https://doi.org/10.1016/s1352-2310(99)00179-x

Lewis, J. M., Kaplan, M. L., Vellore, R., Rabin, R. M., Hallett, J., & Cohn, S. A. (2011). Dust storm over the Black Rock Desert: Larger-scale dynamic signatures. *Journal of Geophysical Research*, *116*, D06113. https://doi.org/10.1029/2010JD014784

Mellor, G. L., & Yamada, T. (1974). A hierarchy of turbulence closure models for planetary boundary layers. *Journal of the Atmospheric Sciences*, *31*(7), 1791–1806. https://doi.org/10.1175/1520-0469(1974)031%3C1791:AHOTCM%3E2.0.CO;2

Mlawer, E. J., Taubman, S. J., Brown, P. D., Iacono, M. J., & Clough, S. A. (1997). Radiative transfer for inhomogeneous atmospheres: RRTM, a validated correlated-k model for the longwave. *Journal of Geophysical Research*, *102*(D14), 16,663–16,682. https://doi.org/10.1029/97JD00237

Moulin, C., Lambert, C. E., Dayan, U., Masson, V., Ramonet, M., Bousquet, P., … Balkanski, Y. J. (1998). Satellite climatology of African dust transport in the Mediterranean atmosphere. *Journal of Geophysical Research*, *103*(D11), 13,137–13,144. https://doi.org/10.1029/98JD00171

Pérez García-Pando, C., Stanton, M., Diggle, P., Trzaska, S., Miller, R. L., Perlwitz, J. P., … Thomson, M. (2014). Soil dust aerosols and wind as predictors of seasonal meningitis incidence in Niger. *Environmental Health Perspectives*, *122*(7), 679–686. https://doi.org/10.1289/ehp.1306640

Perry, K. D., Cahill, T. A., Eldred, R. A., Dutcher, D. D., & Gill, T. E. (1997). Long-range transport of North African dust to the eastern United States. *Journal of Geophysical Research*, *102*(D10), 11,225–11,238. https://doi.org/10.1029/97JD00260

Pokharel, A. K. (2016). Atmospheric dynamics of sub-tropical dust storms, University of Nevada, Reno, ProQuest Dissertations Publishing, 2016. 10161308 Retrieved from: https://search.proquest.com/openview/da62a119163cda173814073c75d3bc4e/1?pq-origsite=gscholar&cbl=18750&diss=y

Pokharel, A. K., Kaplan, M. L., & Fiedler, S. (2016). Atmospheric dynamics of the Harmattan surge on March 2, 2004. *ProScience*, *3*, 84–93. https://doi.org/10.14644/dust.2016.014

Prospero, J. M., & Lamb, P. J. (2003). African droughts and dust transport to the Caribbean: Climate change implications. *Science*, *302*(5647), 1024–1027. https://doi.org/10.1126/science.1089915

Riehl, H., Alaka, M. A., Jordan, C. L., & Renard, R. J. (1954). The jet stream. *Meteorological Monographs* (Vol. 2, No. 7). Boston, MA: American Meteorological Society.

Rinecker, M. M., Suarez, M. J., Gelaro, R., Todling, R., Bacmeister, J., Liu, E., … Schubert, S. D. (2011). MERRA: NASA's modern-era retrospective analysis for research and applications. *Journal of Climate*, *24*(14), 3624–3648. https://doi.org/10.1175/JCLI-D-11-00015.1

Rochette, S. M., & Market, P. S. (2006). A primer on the ageostrophic wind. *National Weather Digest*, *30*, 17–28.

Skamarock, W. C., Klemp, J. B., Dudhia, J., Gill, D. O., Barker, D. M., Duda, M. G., … Powers, J. G. (2008). A description of the Advanced Research WRF version 3, NCAR Tech. Note NCAR/TN-475+STR (113 pp.)

Smolarkiewicz, P. K., & Rotunno, R. (1989). Low Froude number flow past three dimensional obstacles. Part 1: Baroclinically generated lee vortices. *Journal of the Atmospheric Sciences*, *45*, 1872–1905.

Stull, R. B. (2000). *Meteorology for scientists and engineers*. Pacific Grove, CA: Pacific Grove/Brooks Cole.

Swap, R., Garstang, M., Greco, S., Talbot, R., & Kallberg, P. (1992). Saharan dust in the Amazon Basin. *Tellus B*, *44*(2), 133–149. https://doi.org/10.1034/j.1600-0889.1992.t01-1-00005.x

Thompson, G., Field, P. R., Hall, W. D., & Rasmussen, R. M. (2006). A new bulk microphysics parameterization for WRF and MM5. In *Proceedings of the Seventh Weather and Research Forecasting Workshop* (pp. 1–11). Boulder, CO: National Center for Atmospheric Research.

Thompson, G., Rasmussen, R. M., & Manning, K. (2004). Explicit forecasts of winter precipitation using an improved bulk microphysics scheme. Part I: Description and sensitivity analysis. *Monthly Weather Review*, *132*(2), 519–542. https://doi.org/10.1175/1520-0493(2004)132%3C0519:efowpu%3E2.0.co;2.

Todd, M. C., Washington, R., Martins, J. V., Dubovik, O., Lizcano, G., M'Bainayel, S., & Engelstaedtler, S. (2007). Mineral dust emission from the Bodélé Depression, northern Chad, during BoDEx 2005. *Journal of Geophysical Research*, *112*, D06207. https://doi.org/10.1029/2006JD007170

Todd, M. C., Washington, R., Raghavan, S., Lizcano, G., & Knippertz, P. (2008). Regional model simulations of the Bodélé low-level jet of northern Chad during the Bodélé Dust Experiment (BoDEx 2005). *Journal of Climate*, *21*(5), 995–1012. https://doi.org/10.1175/2007JCLI1766.1

Washington, R., & Todd, M. C. (2005). Atmospheric controls on mineral dust emission from the Bode´le´ Depression, Chad: The role of the low level jet. *Geophysical Research Letters*, *32*, L17701. https://doi.org/10.1029/2005GL023597

Washington, R., Todd, M. C., Lizcano, G., Tegen, I., Flamant, C., Koren, I., … Prospero, J. M. (2006). Links between topography, wind, deflation, lakes and dust: The case of the Bode'le´ Depression, Chad. *Geophysical Research Letters*, *33*, L09401. https://doi.org/10.1029/2006GL025827

Yaalon, D. H., & Ganor, E. (1979). East Mediterranean trajectories of dustcarrying storms from the Sahara and Sinai. In C. Morales (Ed.), *Saharan dust: Mobilization, transport, deposition* (pp. 187–193). New York: John Wiley.

Zhang, F. Q., Koch, S. E., Davis, C. A., & Kaplan, M. L. (2000). A survey of unbalanced flow diagnostics and their application. *Advances in Atmospheric Sciences*, *17*(2), 165–183. https://doi.org/10.1007/s00376-000-0001-1